Earth, Planets and Space

EXPRESS LETTER

Open Access

CrossMark

Temporal variation in the resistivity structure of the first Nakadake crater, Aso volcano, Japan, during the magmatic eruptions from November 2014 to May 2015, as inferred by the ACTIVE electromagnetic monitoring system

Takuto Minami[1*] , Mitsuru Utsugi[2], Hisashi Utada[1], Tsuneomi Kagiyama[2,3] and Hiroyuki Inoue[2]

Abstract

During the last magmatic eruption period of Aso volcano (November 2014 to May 2015), a controlled-source electromagnetic volcano monitoring experiment (ACTIVE) was conducted. Here, we interpret the temporal variations in the electromagnetic responses. The ACTIVE system installed at the first Nakadake crater, the only active crater of Aso, consisted of a transmitter located northwest of the crater and four (before the eruptions) or three (after the eruptions) vertical induction coil receiver stations. The ACTIVE system succeeded in detecting temporal variations in the resistivity structure during the latest magmatic eruption period. The response amplitude started to increase in November 2014, peaked in February 2015, and decreased slightly in August 2015. An unstructured tetrahedral finite element three-dimensional inversion that accounted for topographic effects was used to interpret temporal variations in the ACTIVE response. The 3-D inversion results revealed that temporal variations in the ACTIVE response are attributed mainly to (1) a broad increase in resistivity at elevations from 750 to 850 m, not only directly beneath the crater bottom but also outside the crater, and (2) a thin layer of decrease in resistivity at the elevation of ~ 1000 m on the western side of the crater. The increase in resistivity can be ascribed to a decrease in the amount of conductive groundwater in the upper part of an aquifer located below the elevation of 800 m, while the decrease in resistivity implies that enhanced fluid temperature and pressure changed the subsurface hydrothermal system and formed a temporal fluid reservoir at the shallow level during the magmatic eruption period.

Keywords: Aso volcano, ACTIVE, Resistivity structure, Magma, Eruption, Monitoring, Controlled source

Introduction

Aso volcano

Aso volcano, which is located in the center of Kyushu Island, is one of the most active volcanoes in Japan (Fig. 1a). The first Nakadake crater of Aso volcano is known to have an activity cycle of 15–20 years, in which ash emissions and Strombolian eruptions typically follow a lowering of the water level of the crater lake (Kawakatsu et al. 2000). The loss of water from the crater lake, therefore, can be a proxy that indicates when volcanic activity is increasing, although water level drops in 2003 and 2011 were not followed by magmatic activity. In July 2014, the crater lake dried up, and the latest magmatic eruptions started on November 25, 2014. To achieve full understanding of the volcanic cycle and the subsurface

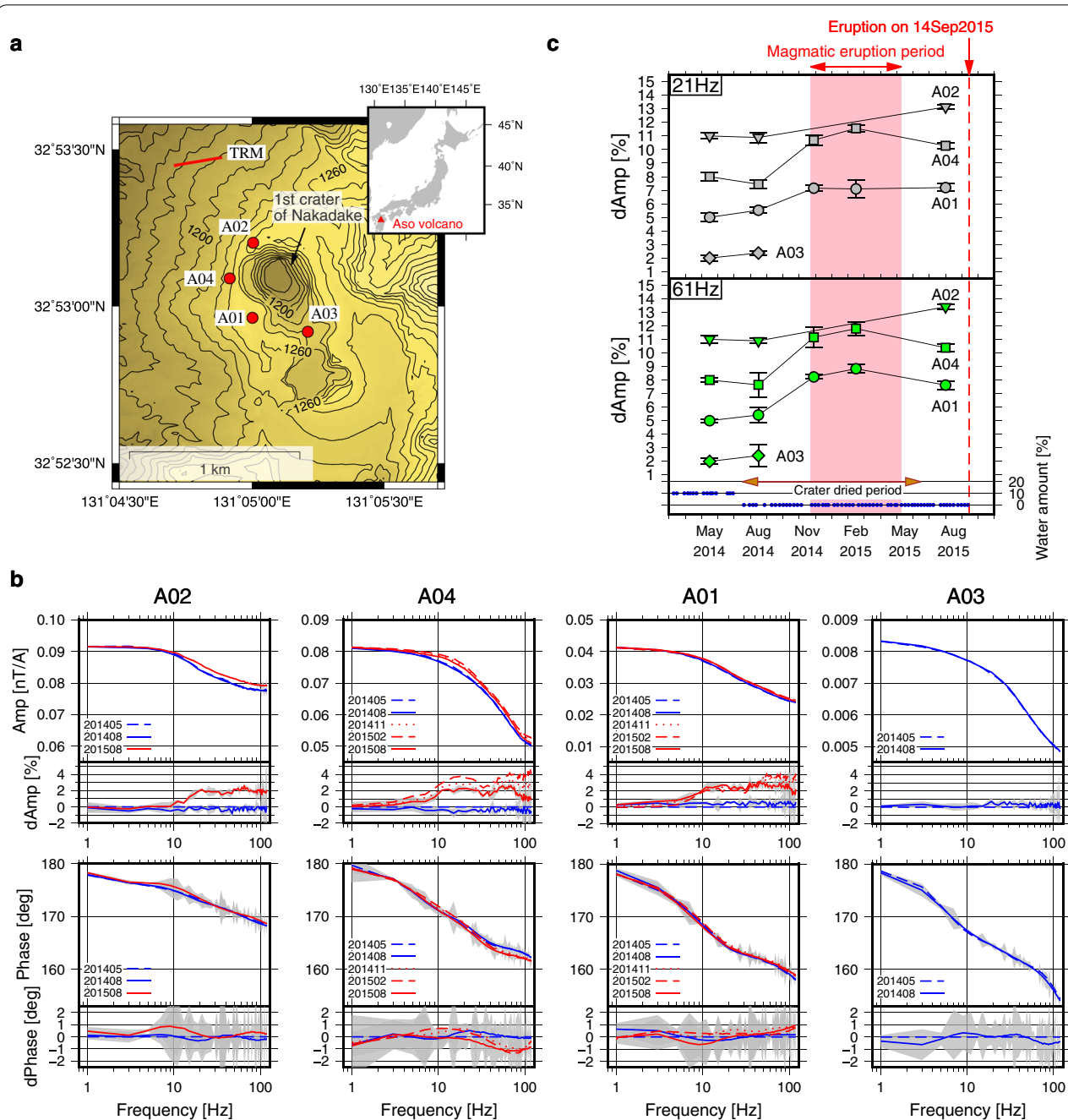Minami *et al. Earth, Planets and Space* (2018) 70:138

Page 2 of 10

Fig. 1 ACTIVE observation configuration and obtained responses. **a** Location of Aso volcano and ACTIVE system installed in May 2014 are shown. TRM and A01 to A04 indicate the transmitter and receivers, respectively. **b** In each panel, upper plots show amplitudes of the ACTIVE response and differences in percent from the values in May 2014, while lower plots depict phases and their differences in degrees from those in May 2014 again. The blue and red lines mean the responses before and after magmatic eruptions began on November 25, 2014, respectively. Only for the responses in August 2014 and August 2015, observation errors are drawn in gray. **c** Time variations of amplitude are plotted for 21 Hz and 61 Hz. The water amount of the crater lake (measured as the area ratio of the lake surface to the whole crater bottom) is plotted by blue dots (Japan Meteorological Agency 2016), where 100% means the lake surface covering the whole crater bottom

Minami *et al. Earth, Planets and Space* (2018) 70:138

Page 3 of 10

system, the activity of Aso volcano should be monitored by multiple methods.

Previous studies have revealed several important features of the system providing magma to the first Nakadake crater of Aso volcano. A magma chamber that feeds magma to the crater is inferred to be located 3 km west of the Nakadake craters at a depth of 5–6 km (Sudo and Kong 2001). Hata et al. (2016) created a three-dimensional (3-D) resistivity model using magnetotelluric data and imaged a north-dipping reservoir and magma pathway under the Nakadake craters extending to a depth of more than 10 km. Broadband seismic observations have shown that long-period (~ 15 s) tremors around Nakadake can be attributed to isotropic expansion and contraction accompanying inflation and deflation of an inclined tensile crack with a strike that is sub-parallel to the chain of Nakadake craters (Yamamoto et al. 1999). Kanda et al. (2008) created a two-dimensional (2-D) resistivity model from audio-frequency magnetotelluric (AMT) data (2004–2005) that implies the presence of a conductive clay cap below the crater and hydrothermal fluid reservoir underneath.

For monitoring volcanic activity, Ichimura et al. (2018) developed a method for tracking the source locations of continuous tremors before ash and gas emissions. Terada et al. (2012) showed that changes in the shallow hydrothermal system can be tracked by monitoring enthalpy and mass flux to the crater lake. It is also desirable to monitor subsurface electrical resistivity, which is sensitive to the pore fluid/magma conductivity (e.g., Hermance 1995; Gaillard 2004).

ACTIVE (Array of Controlled Transient-electromagnetics for Imaging Volcano Edifice; Utada et al. 2007) is an electromagnetic (EM) volcano monitoring system that utilizes a transient EM (TEM) technique. This technique, in which the decay time of the vertical magnetic component after the horizontal electrical source is switched off is measured, has been used previously in other volcanic settings (e.g., Srigutomo et al. 2008). The ACTIVE system, which was installed around the first Nakadake crater in May 2014, consists of a transmitter, which transmits a square-wave electric current into the ground via two electrodes, and an array of induction coil receivers, which observe the vertical component of the induced magnetic field (Fig. 1a). During the latest series of magmatic eruptions, from November 2014 to May 2015, the ACTIVE system succeeded in detecting large temporal variations in its response that corresponded to the start time of the magmatic eruptions. In this study, we performed 3-D inversions to model the temporal variations in the ACTIVE responses during the magmatic eruption period.

Magmatic eruptions of Aso volcano from November 2014 to May 2015

Magmatic eruptions of Aso volcano started on November 25, 2014, about 20 years after previous series of magmatic events. The eruptions mainly consisted of ash eruptions (Ono et al. 1995), but Strombolian eruptions ejecting incandescent fragments without any ashes also occurred intermittently (Yokoo and Miyabuchi 2015). The chemical composition of the ash ejected during this period was similar to that of ash ejected during previous magmatic eruptions in April 1990 and September 1979 (Miyabuchi et al. 2018). In conjunction with the magmatic activity, fallout of fragile, light yellow deliquescent materials (salt shells) was observed. These materials were compositionally similar to that of the salt that forms when the crater lake water evaporates and likely resulted from the interaction of hydrothermal fluids with magma in the conduit (Shinohara et al. 2018). In early May 2015, the crater bottom subsided and the magmatic eruptions stopped (Japan Meteorological Agency 2015), although the activity did not cease completely and a phreatomagmatic eruption took place on September 14, 2015 (Miyabuchi et al. 2018).

Data

ACTIVE responses were recorded during observation campaigns in May 2014, August 2014, November 2014, February 2015, and August 2015. The transmitter current had a square wave form with a period of 1 s. Figure 1b shows the amplitude and phase of the ACTIVE response, namely the vertical component of the magnetic field divided by the source electric current. The errors of the responses were obtained by stacking responses from segments with a duration of 1 s. Very few responses were obtained from the A02 and A03 receivers after November 2014 because it was difficult to reach these receiver sites after the magmatic eruptions began.

The amplitudes at receiver sites A04, A02, and A01 clearly increased in the frequency range higher than 10 Hz after the magmatic eruptions started in November 2014 (Fig. 1b). Between May 2014 and August 2015, the amplitudes increased by ~ 2%, and the increase was larger than the error except in the frequency range above 80 Hz. In contrast, magnitude of temporal variations of the phase was lower than the error in the whole frequency range. Because almost no temporal variations of amplitude were observed in the 1–5 Hz frequency range, we can assume that there were no temporal variations in the background resistivity structure corresponding to that frequency range. The 2-D AMT analysis by Kanda et al. (2008) showed that the background resistivity beneath the Nakadake craters is ~ 50 Ωm. Because the skin depth at 5 Hz in a 50 Ωm medium, 1.58 km, is close to the

Minami *et al. Earth, Planets and Space* (2018) 70:138

Page 4 of 10

summit elevation of the central cones of Aso volcano, we decided to limit the model space for our inversions to elevations higher than 0 m, which we expected to stabilize inversions conducted with small datasets.

At both A04 and A01, temporal variations of amplitude were observed during the magmatic eruption period (MEP; November 2014 to May 2015) (Fig. 1b). At A04, there were two temporal variation peaks, at frequencies of $\sim$20 and $\sim$60 Hz. The difference from May 2014 was largest in February 2015 ($\sim$4% at 20 and 60 Hz), whereas the difference was slightly smaller in August 2015 than it was in November 2014 (dAmp plots of the A04 panel in Fig. 1b). The large difference in February 2015 can be attributed to enhanced magmatic activity during MEP, and the existence of temporal variation peaks at fixed frequencies implies that resistivity changes occurred in the same zone both during and after MEP. The increases in amplitude at 20 and 60 Hz suggest increases in resistivity at 0.79 km and 0.46 km depths, respectively, given the skin depths in a 50 Ωm medium. At A01, in contrast, temporal variations were not clear at 20 Hz during MEP, while the amplitude decreased from February 2015 to August 2015 at the frequency higher than 60 Hz.

The time variations of the amplitude at 21 and 61 Hz (Fig. 1c) show that, at A01 and A04, the amplitudes were higher at these frequencies during MEP, and kept higher levels after MEP than those before MEP. We selected the datasets from August 2014 and August 2015 to examine temporal variations in the resistivity structure due to the magmatic activity of Nakadake. The water level of the crater lake was very low throughout the five observation campaigns, and the lake was completely dry from July 2014 to June 2015 (Japan Meteorological Agency 2016). We assumed no water in the crater lake in the inversion models. The inversion method adopted is described in the next section.

Method

Inversion algorithm

We conducted 3-D inversions to infer the resistivity structure corresponding to the ACTIVE responses; for these inversions, we used the finite element (FE) method with an unstructured tetrahedral mesh. In this section, we describe essential parts of our inversion method.

In the forward part, we solve the vector Helmholtz equation in terms of the magnetic vector potential A,

$$\nabla \times (\nabla \times A) + i\omega\mu\hat{\sigma}A = \mu i_s, \tag{1}$$

by the edge-based FE method (e.g., Yoshimura and Oshiman 2002). Here, ω is the angular frequency, μ is the magnetic permeability, and $\hat{\sigma}$ ($\equiv \sigma + i\omega\varepsilon$) is the complex conductivity, where σ is the electrical conductivity and ε is the electric permittivity; μ and ε are assumed to be free-space values throughout this paper. i_s denotes the source electric current density. The electric and magnetic fields, E and B, respectively, are linked to A by the relationships $E = -i\omega A$ and $B = \nabla \times A$ (see Yoshimura and Oshiman 2002 for the reason why the scalar potential ϕ is omitted). Equation (1) is first discretized by the FE method with first-order tetrahedral elements and then solved by the weighted residuals method. For the source term in Eq. (1), we adopt a kind of Heaviside function, where i_s has a constant value only on a straight line within an element (e.g., Ansari and Farquharson 2014). To include the actual topography, we adopt an unstructured tetrahedral mesh generated by Gmsh freeware (http://gmsh.info/).

In the inverse part, we minimize the objective function,

$$\Phi(\mathbf{m}) = \Phi_d(\mathbf{m}) + \lambda\Phi_m(\mathbf{m}), \tag{2}$$

$$\Phi_d(\mathbf{m}) = \frac{1}{2}(F(\mathbf{m}) - d)^T B_d(F(\mathbf{m}) - d), \tag{3}$$

$$\Phi_m(\mathbf{m}) = \frac{1}{2}(\mathbf{m} - \mathbf{m}_{ref})^T B_m(\mathbf{m} - \mathbf{m}_{ref}), \tag{4}$$

where λ is a trade-off parameter and d is a data vector consisting of amplitudes and phases of ACTIVE responses. $F(\mathbf{m})$ is the vector resulting from the forward modeling; B_d is a diagonal weighting matrix consisting of the reciprocals of the squared standard errors; $\mathbf{m}$ is the model vector, defined as $m_i = \log_{10}\rho_i$ in this paper, where ρ_i is the resistivity of the i-th model block, and $\mathbf{m}_{ref}$ is the reference model. For the roughening matrix B_m, we adopt $B_m = R^T R$ following Usui et al. (2017). The i-th component of the product of R and $\mathbf{m}$ is given by,

$$[R\mathbf{m}]_i = \sum_{j}^{N_{if}} (m_i - m_j), \tag{5}$$

where N_{if} is the number of model blocks neighboring the i-th model block. Note that R is a kind of Laplacian operator for an unstructured tetrahedral mesh (e.g., see the analogous form of R_2 in Eq. (2) of Constable et al. 1987).

Equation (2) is minimized by using the Gauss–Newton scheme with a data-space approach (e.g., Siripunvaraporn et al. 2005). For the selection of λ, a cooling strategy (e.g., Schwarzbach and Haber 2013) is adopted, in which λ is decreased by a factor of $10^{1/3}$ when nRMS = $\sqrt{2\Phi_d(\mathbf{m})/N_d}$, where N_d is the length of d, does not decrease by 10% from the previous iteration step.

Minami *et al. Earth, Planets and Space* (2018) 70:138

Page 5 of 10

Inversions of the ACTIVE datasets from August 2014 to August 2015

We conducted two inversions of ACTIVE datasets, one of the dataset obtained in August 2014, before MEP, and the other dataset obtained in August 2015, after MEP. Because the peak frequencies of temporal variations of the ACTIVE response were similar from November 2014 onward (Fig. 1b), we can infer the temporal variations in the resistivity structure between the period before and that after the magmatic eruptions began from the difference between August 2014 and August 2015. Datasets from four receivers were available for August 2014, but for August 2015, datasets from only three receivers were available. Therefore, we first inverted the four receiver datasets for August 2014 to obtain model $\mathbf{m}_0$, and then we inferred model $\mathbf{m}_1$ by inverting the three receiver datasets for August 2015. The relationship between $\mathbf{m}_0$ and $\mathbf{m}_1$ is expressed as,

$$\mathbf{m}_1 = \mathbf{m}_0 + d\mathbf{m},$$

where $d\mathbf{m}$ corresponds to the temporal variation in the resistivity structure between August 2014 and August 2015. For the $\mathbf{m}_0$ inversion, we adopted a modified version of the 3-D resistivity structure obtained by the AMT survey in 2004–2005 (Kanda et al. 2015) as the initial model (see Additional file 1: Fig. S1 and Additional file 1: Fig. S2 for our tetrahedral mesh and the initial model, respectively) and a homogeneous 100 Ωm structure as the reference model in Eq. (4). For the $\mathbf{m}_1$ inversion, $\mathbf{m}_0$ was used for both the initial and reference models. In both the $\mathbf{m}_0$ and $\mathbf{m}_1$ inversions, $\boldsymbol{B}_d$ consisted of the real measurement errors with error floors of 1% and arcsin $(0.01) * 180/\pi = 0.573$ degrees for the amplitude and phase, respectively.

Because the available datasets were not adequate in our 3-D inversions, we limited the model space for the $\mathbf{m}_0$ inversion vertically to elevations higher than 0.0 m and laterally to a 3 km × 3 km square centered on the first Nakadake crater; outside of this zone, all model blocks were integrated into a single model block corresponding to a homogeneous background medium, which was also determined by the $\mathbf{m}_0$ inversion. In the $\mathbf{m}_1$ inversion, the background resistivity of $\mathbf{m}_1$ was fixed to that of $\mathbf{m}_0$, because only three receiver datasets were available.

Results

The $\mathbf{m}_0$ and $\mathbf{m}_1$ inversions were successfully completed by the described method. The initial value of λ in Eq. (2) was set to 1.0 in the $\mathbf{m}_0$ inversion and to 5.0 in the $\mathbf{m}_1$ inversion. In selecting λ, we found that values smaller than these made the inversion results unstable, whereas larger ones did not appreciably change the results with increased iterations. The RMS misfits of the final $\mathbf{m}_0$ and

$\mathbf{m}_1$ models resulted in nRMS values of 1.39 and 1.23, respectively. See Additional file 1: Fig. S3 for the final fits of the two inversions. In the remainder of this section, we describe the features of $\mathbf{m}_0$, $\mathbf{m}_1$, and $d\mathbf{m}$ (Figs. 2, 3, and 4). In these figures, zones which do not affect nRMS much are masked (shown in gray) based on sensitivity thresholds. Refer to Additional file for the selection of thresholds and the sensitivity distributions in $\mathbf{m}_0$ and $\mathbf{m}_1$ (Additional file 1: Figs. S4–S6).
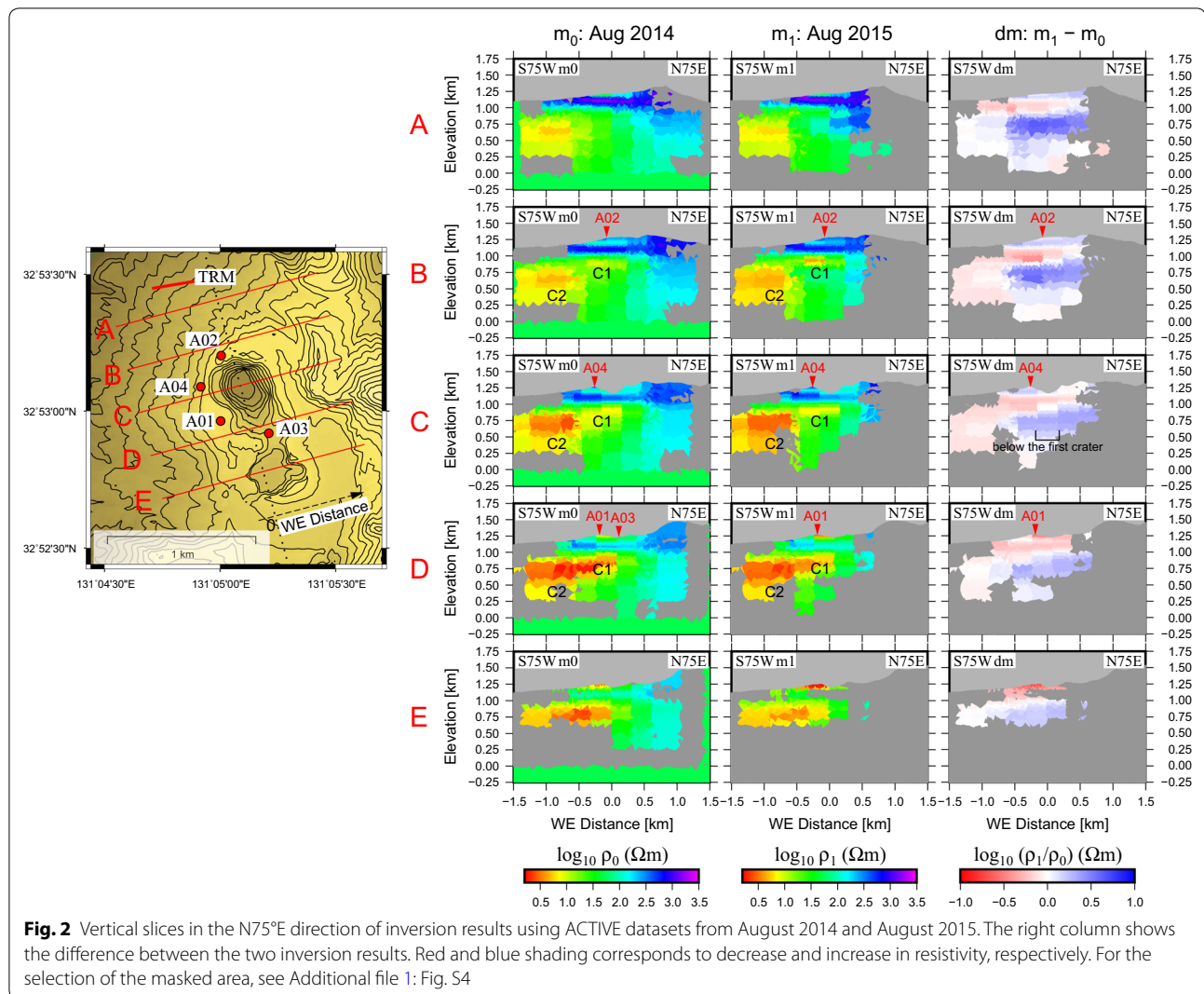
Figure 2 shows the inversion results in vertical sections oriented in the N75°E direction, which is the same orientation adopted by Kanda et al. (2008) for the 2-D AMT analysis. In the $\mathbf{m}_0$ model, a shallow conductive anomaly, C1, was imaged at elevations from 800 to 1000 m on the western side of the first crater, while a deep conductive anomaly, C2, was imaged at the west of C1 at elevations from 250 to 800 m (Fig. 2 sections B, C, and D; left panels). The shallow and deep anomalies correspond to the C1 and C2 anomalies imaged by Kanda et al. (2008). In $d\mathbf{m}$, an increase in resistivity (blue shading) is apparent in all sections at elevations from 500 to 1000 m, and in sections B, C, and D, a thin layer of conductive change (red shading) is visible at an elevation of ~1050 m below and on the western side of the crater (Fig. 2, right panels).

The vertical sections shown in Fig. 3 are oriented in the N15°W direction, parallel to the orientation of the crater chain. Compared with $\mathbf{m}_0$ (left panels), the resistivity of C2 decreased slightly in $\mathbf{m}_1$. In $d\mathbf{m}$, resistivity increases also appear at elevations of 500–1000 m, as in Fig. 2. It is noticeable that in the $d\mathbf{m}$ results shown in Figs. 2 and 3, the resistive variation has a peak elevation of ~750 m and is not limited to the zone below the first crater but extends laterally to outside of the crater.

We also examined the inversion results in horizontal sections at elevations between 500 and 1050 m (Fig. 4), where the sections at 650, 750, and 850 m show the C2 anomaly. At elevations from 650 to 850 m, resistive variation is observed not only below the crater but also outside of the crater. We confirmed that the peak elevation of the resistive variation, ~750 m, was not affected by the vertical limit imposed on the model space by conducting another inversion in which the model space was extended downward to −600 m. At an elevation of ~1050 m, conductive variation is recognized on the western side of the crater.

Discussion

We developed a conceptual model to explain the causes of the resistivity variations under the first Nakadake crater of Aso volcano (Fig. 5). Kanda et al. (2008) showed that, before volcanic explosions of Aso volcano, a preparation zone composed of a hydrothermally altered clay cap and a high-pressure hydrothermal fluid
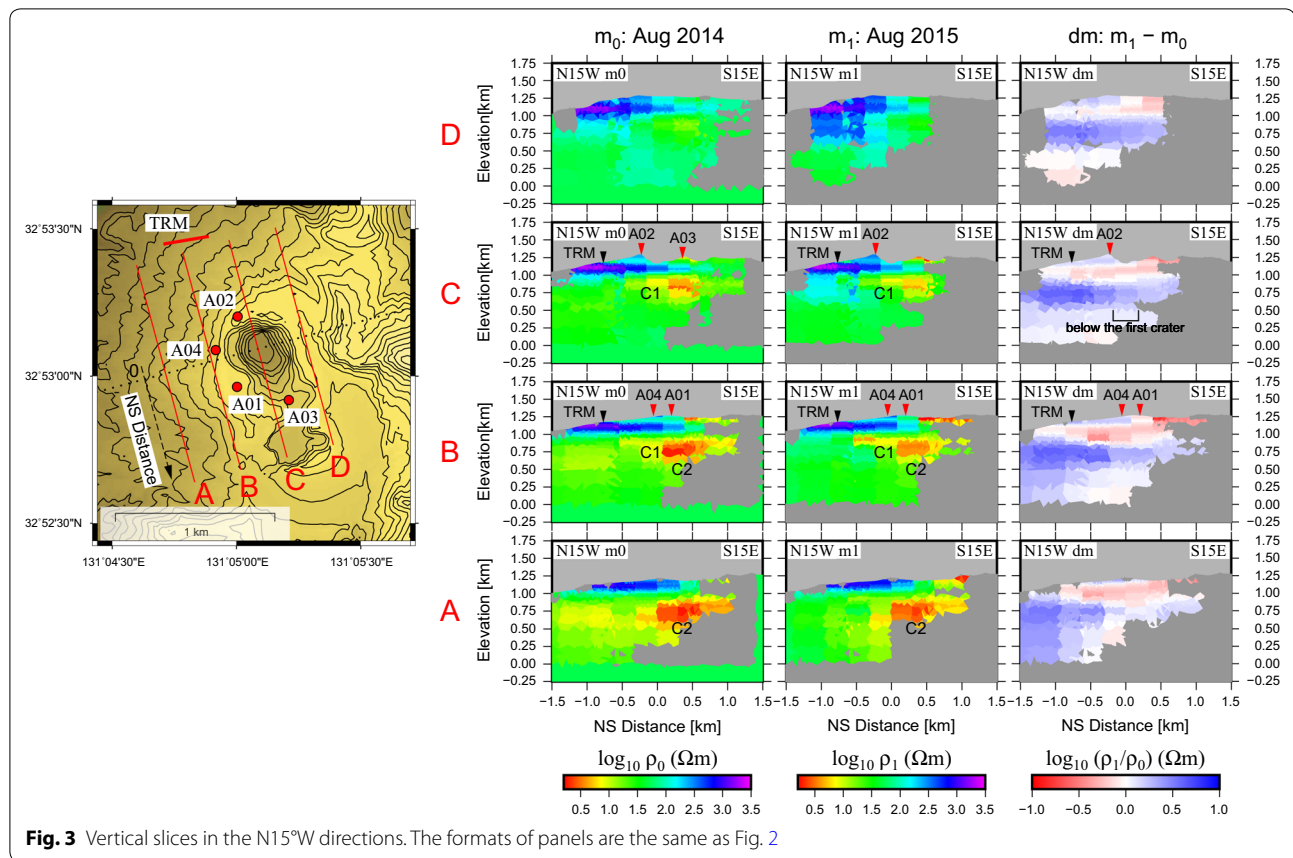
Minami *et al. Earth, Planets and Space*   (2018) 70:138

Page 6 of 10

Fig. 2 Vertical slices in the N75°E direction of inversion results using ACTIVE datasets from August 2014 and August 2015. The right column shows the difference between the two inversion results. Red and blue shading corresponds to decrease and increase in resistivity, respectively. For the selection of the masked area, see Additional file 1: Fig. S4

reservoir is located just beneath the crater bottom and adjacent to hydrothermally altered rock on the western side of the crater (Fig. 5a). C1 in this study corresponds to the altered rock and the preparation zone beneath the crater bottom. Before magmatic eruptions, gases and liquid are inferred to be supplied to the crater bottom through a crack conduit (Yamamoto et al. 1999) and then via narrower fluid paths in the preparation zone.

After magmatic eruptions begin, it is expected that resistivity increases just below the crater because the eruptions break and eject the clay cap, and because the amount of hydrothermal fluid is decreased by the enhanced pressure and temperature (Fig. 5b). However, a consistent increase in resistivity is not seen in the results just below the crater (Fig. 3 section C). Because there were no receivers within the crater, temporal variations are difficult to detect directly beneath the crater bottom.

Instead, our inversion analysis revealed a thin layer of decrease in resistivity at an elevation of ~ 1050 m on the western side of the crater (1050 m section, Fig. 4). We deduce that this resistivity decrease corresponds to a temporal fluid reservoir formed during MEP. The high pressure due to increasing fluid temperature below the crater bottom possibly evacuated hydrothermal fluid to outside of the preparation zone, or interfered with water supply from rainfall to the existing reservoir and to deep aquifer. Both scenarios can cause a temporal reservoir at the shallow level (Fig. 5b). This temporal reservoir might be associated with the phreatomagmatic eruption on September 14, 2015.

Below the elevation of C1, a clear increase in resistivity was laterally broad at elevations of 650–850 m and was present not only below the crater bottom but also outside the crater. We speculate that this resistivity increase was caused by a decrease in the groundwater content of

Minami *et al. Earth, Planets and Space* (2018) 70:138

Page 7 of 10

Fig. 3 Vertical slices in the N15°W directions. The formats of panels are the same as Fig. 2

the aquifer underlying Nakadake (Fig. 5b). In their 2-D model, Kanda et al. (2008) imaged conductive anomalies caused by the presence of an aquifer (or altered rock) at elevations lower than 800 m. Because we observed a resistive variation peak at elevations from 750 to 850 m, the water content decreased mainly in the upper part of the aquifer, probably as a result of the generation of hot gases. Although the resistivity of upwelling magma that triggered magmatic eruptions was 1–10 Ωm (e.g., Gaillard 2004), consistent anomaly was not imaged below the preparation zone in m_1. This is because magma filling the crack conduit could not reduce the bulk resistivity for the low conduit thickness of ~25 m (Yamamoto 2005).

Strictly speaking, m_1 reflects not a stage during MEP but a transition stage from the high magmatic activity (February 2015) to the phreatomagmatic eruption (September 2015). The amplitudes at A01 and A04 decreased by < 2% from February to August in 2015 with temporal variation peaks at fixed frequencies (Fig. 1b, c). We,
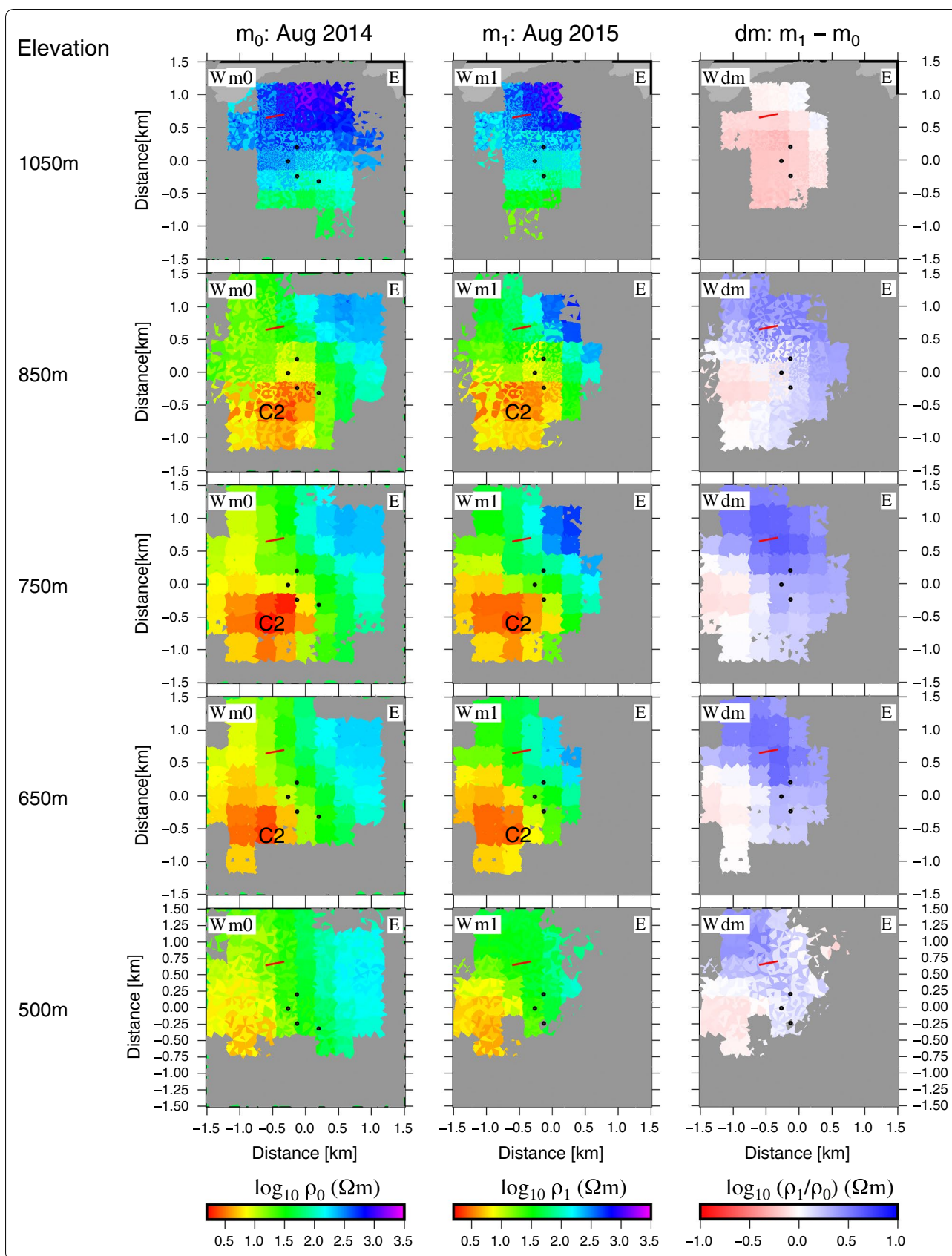
therefore, infer that the resistivity structure in February 2015 was close to m_1 and was more resistive as a whole. This leads to the fact that the subsurface hydrothermal system dried to a high degree in February and regained fluid by August, before the phreatomagmatic eruption in September. Shinohara et al. (2018) observed fallout of salt shell in January to March 2015, implying the presence of hydrothermal fluid even during MEP. An impermeable hot shield zone might isolate the magma path from the hydrothermal fluid (Fig. 5b), thus preventing phreatic eruptions from occurring during MEP.

Conclusion

In this paper, we reported ACTIVE responses indicating temporal variations in the resistivity structure below the first Nakadake crater during MEP (from November 2014 to May 2015), and we interpreted them by conducting 3-D inversions using a FE method with an unstructured tetrahedral mesh. Our inversions of

(See figure on next page.)
Fig. 4 Horizontal slices of the inversion results. The formats of the panels are similar to those of Figs. 2 and 3. The black dots in panels depict the locations of four receivers shown in Fig. 1, while a red line shows the source electric wire
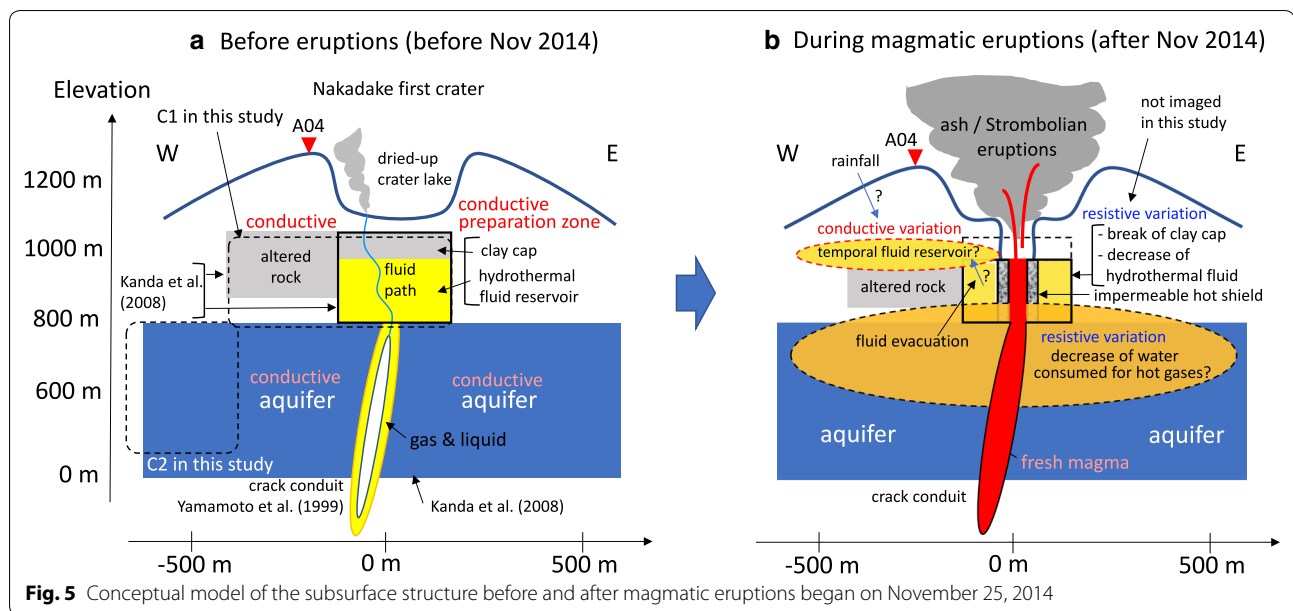
Minami *et al. Earth, Planets and Space* (2018) 70:138

Page 8 of 10

Minami *et al. Earth, Planets and Space*   (2018) 70:138

Page 9 of 10

Fig. 5 Conceptual model of the subsurface structure before and after magmatic eruptions began on November 25, 2014

the ACTIVE datasets from August 2014 (before MEP) and August 2015 (after MEP) succeeded in revealing temporal variations in the resistivity structure between the period before and that after the magmatic eruptions began in November 2014. We observed a noticeable decrease in resistivity at an elevation of ~ 1050 m on the western side of the crater, and an increase in resistivity at elevations of 750 to 850 m, not only below the crater bottom but also extending outside of the crater. The shallow conductive variation may be ascribed to formation of a temporal fluid reservoir due to high fluid pressure around the preparation zone. The deep resistive variation was probably caused by a decrease in the amount of conductive groundwater in the upper part of the aquifer imaged by the previous 2-D AMT analysis due to enhanced pressure and temperature in the vicinity of the magma conduit and by the generation of hot gases.

Our results showed that the temporal variations of a TEM dataset can be effectively modeled by a full 3-D inversion even when there are only three or four receiver sites, given sufficient a priori information. In this study, this information was provided by an initial 3-D resistivity model. Our results demonstrated that the ACTIVE system can efficiently monitor volcanic activity and hydrothermal systems beneath volcanoes.

Additional file

Additional file 1. Details of inversions and sensitivity analyses.

Authors' contributions
TM, MU, and HI participated in acquisition of ACTIVE data. MU processed the obtained ACTIVE data. TM conducted 3-D inversions and drafted the manuscript. UM, HU, and TK contributed to the planning of this study and interpretation of the data. All authors read and approved the final manuscript.

Author details
[1] Earthquake Research Institute, The University of Tokyo, 1-1-1 Yayoi, Bunkyo-ku, Tokyo 113-0032, Japan. [2] Aso Volcanological Laboratory, Institute for Geothermal Sciences, Graduate School of Science, Kyoto University, 3028 Sakanashi, Ichinomiya-cho, Aso-shi, Kumamoto 869-2611, Japan. [3] Present Address: Aso Volcano Museum, 1930-1 Akamizu, Aso-shi, Kumamoto 869-2232, Japan.

Publisher's Note
Springer Nature remains neutral with regard to jurisdictional claims in published maps and institutional affiliations.

Minami *et al. Earth, Planets and Space* (2018) 70:138

Page 10 of 10

References

Ansari S, Farquharson CG (2014) 3D finite-element forward modeling of electromagnetic data using vector and scalar potentials and unstructured grids. Geophysics 79:E149–E165. https://doi.org/10.1190/geo2013-0172.1

Constable SC et al (1987) Occam's inversion: a practical algorithm for generating smooth models from electromagnetic sounding data. Geophysics 52:289–300. https://doi.org/10.1190/1.1442303

Gaillard F (2004) Laboratory measurements of electrical conductivity of hydrous and dry silicic melts under pressure. Earth Planet Sci Lett 218(1–2):215–228. https://doi.org/10.1016/S0012-821X(03)00639-3

Hata M et al (2016) Crustal magma pathway beneath Aso caldera inferred from three-dimensional electrical resistivity structure. Geophys Res Lett 43:10720–10727. https://doi.org/10.1002/2016GL070315

Hermance JF (1995) Electrical conductivity models of the crust and mantle. AGU Ref. Shelf 1, Global Earth Phys., Handbook of Phys. Constants, pp. 190–205.

Ichimura M et al (2018) Temporal variation in source location of continuous tremors before ash-gas emissions in January 2014 at Aso volcano, Japan. Earth Planets Space 70:125. https://doi.org/10.1186/s40623-018-0895-4

Japan Meteorological Agency (2015) Report of general condition of Aso volcano. Rep Coord Comm Predict Volcan Erupt 132:3–22 **(in Japanese)**

Japan Meteorological Agency (2016) Report of general condition of Aso volcano. Rep Coord Comm Predict Volcan Erupt 136:32–68 **(in Japanese)**

Kanda W, et al (2015) Hydrothermal system around the active crater of Aso volcano inferred from a three-dimensional resistivity structure. Paper presented at Japan Geoscience Union Meeting 2015, Chiba, Japan, 24–28 May 2015

Kanda W et al (2008) A preparation zone for volcanic explosions beneath Naka-dake crater, Aso volcano, as inferred from magnetotelluric surveys. J Volcanol Geotherm Res 178:32–45. https://doi.org/10.1016/j.jvolgeores.2008.01.022

Kawakatsu H et al (2000) Aso94: Aso seismic observation with broadband instruments. J Volcanol Geotherm Res 101:129–154. https://doi.org/10.1016/S0377-0273(00)00166-9

Miyabuchi Y et al (2018) The September 14, 2015 phreatomagmatic eruption of Nakadake first crater, Aso Volcano, Japan: Eruption sequence inferred from ballistic, pyroclastic density current and fallout deposits. J Volcanol Geotherm Res 351:41–56. https://doi.org/10.1016/J.JVOLGEORES.2017.12.009

Ono K et al (1995) Ash eruption of the Naka-dake crater, Aso volcano, southwestern Japan. J Volcanol Geotherm Res 66:137–148. https://doi.org/10.1016/0377-0273(94)00061-K

Schwarzbach C, Haber E (2013) Finite element based inversion for time-harmonic electromagnetic problems. Geophys J Int 193:615–634. https://doi.org/10.1093/gji/ggt006

Shinohara H et al (2018) Salt shell fallout during the ash eruption at the Nakadake crater, Aso volcano, Japan: evidence of an underground hydrothermal system surrounding the erupting vent. Earth Planets Space 70(1):46. https://doi.org/10.1186/S40623-018-0798-4

Siripunvaraporn W et al (2005) Three-dimensional magnetotelluric inversion: data-space method. Phys Earth Planet Inter 150:3–14. https://doi.org/10.1016/j.pepi.2004.08.023

Srigutomo W et al (2008) Resistivity structure of Unzen Volcano derived from time domain electromagnetic (TDEM) survey. J Volcanol Geotherm Res 175:231–240. https://doi.org/10.1016/J.JVOLGEORES.2008.03.033

Sudo Y, Kong L (2001) Three-dimensional seismic velocity structure beneath Aso Volcano, Kyushu, Japan. Bull Volcanol 63:326–344. https://doi.org/10.1007/s004450100145

Terada A et al (2012) A water flow model of the active crater lake at Aso volcano, Japan: fluctuations of magmatic gas and groundwater fluxes from the underlying hydrothermal system. Bull Volcanol 74:641–655. https://doi.org/10.1007/s00445-011-0550-4

Usui Y et al (2017) Three-dimensional resistivity structure of Asama Volcano revealed by data-space magnetotelluric inversion using unstructured tetrahedral elements. Geophys J Int 208:1359–1372. https://doi.org/10.1093/gji/ggw459

Utada H et al (2007) ACTIVE system for monitoring volcanic activity: a case study of the Izu-Oshima Volcano, Central Japan. J Volcanol Geotherm Res 164:217–243. https://doi.org/10.1016/j.jvolgeores.2007.05.010

Yamamoto M (2005) Volcanic fluid system inferred from broadband seismic signals. PhD thesis, University of Tokyo, Tokyo

Yamamoto M et al (1999) Detection of a crack-like conduit beneath the active crater at Aso Volcano Japan. Geophys Res Lett 26:3677–3680. https://doi.org/10.1029/1999GL005395

Yokoo A, Miyabuchi Y (2015) Eruption at the Nakadake 1st crater of Aso volcano started in November 2014. Bull Volcanol Soc Jpn 60:275–278. https://doi.org/10.18940/kazan.60.2_275

Yoshimura R, Oshiman N (2002) Edge-based finite element approach to the simulation of geoelectromagnetic induction in a 3-D sphere. Geophys Res Lett 29:1039. https://doi.org/10.1029/2001GL014121